Tectonophysics 871 (2024) 230191

Contents lists available at ScienceDirect

Tectonophysics

journal homepage: www.elsevier.com/locate/tecto

Identifying the fracture characteristics that control deformation localization and catastrophic failure in fluid-saturated crystalline rocks in upper crustal conditions

Jessica McBeck [a,*], Benoît Cordonnier [b], Yehuda Ben-Zion [c], François Renard [a,d]

[a] Njord Centre, Department of Physics and Geosciences, University of Oslo, Oslo, Norway
[b] European Synchrotron Radiation Facility, Grenoble, France
[c] Department of Earth Sciences and Southern California Earthquake Center, University of Southern California, Los Angeles, CA, USA
[d] Université Grenoble Alpes, Université Savoie Mont Blanc, Université Gustave Eiffel, CNRS, IRD, ISTerre, 38000 Grenoble, France

ARTICLE INFO

Keywords:
Fractures
Localization
Catastrophic failure
Machine learning
X-ray tomography

ABSTRACT

Previous studies show that the total volume of fractures increases non-linearly during loading as rocks approach failure in triaxial compression at stress and temperature conditions representative of the upper crust. However, the factors that control the critical volume of fractures or the critical spatial organization of the fracture network that trigger macroscopic failure remain unclear. To identify the fracture characteristics that determine the timing of macroscopic failure and localization of the fracture networks, we analyze data from six X-ray tomography experiments on Westerly granite with varying confining stress, fluid pressure, and amounts of preexisting damage. We develop machine learning models to predict 1) the timing of failure, 2) the localization of the fracture networks as measured with the Gini coefficient of the fracture volume, and 3) the change in localization from one differential stress step to the next. When the models only have access to individual fracture characteristics, the fracture length produces the best predictions of the distance to failure. When the models have access to the fracture length and sets of other characteristics, the fracture volume, aperture, and distance between fractures produce the best predictions of the distance to failure. The characteristics that describe the time or loading in the experiment, the axial strain and differential stress, produce some of the best predictions of the Gini coefficient. The results are generally consistent among the different experiments, suggesting that the fracture characteristics that determine the timing of macroscopic failure, and the localization of the fracture network, are independent of the range of confining stress, fluid pressure, and amount of preexisting damage tested here. Our results are consistent with the idea that monitoring the spatial distribution of deformation and changes in the seismic wave properties indicative of fracture growth may improve forecasting efforts of failure in the crust.

1. Introduction

Developing a method to estimate the stress conditions at macroscopic failure using characteristics of fracture networks would be a significant advance in our understanding of rock deformation. In tension under constant or increasing stress loading, fracture growth tends to develop unstably, producing rapid macroscopic, system-size failure after initiation. This unstable growth occurs because increasing fracture length increases the stress intensity factor in these systems, and thereby promotes additional fracture growth (e.g., Bieniawski, 1968). Under constant displacement or slow velocity loading, fracture growth in tension can be stable (e.g., Obreimoff, 1930). In compression, experiments show that fractures can grow quasi-stably as the system accumulates more axial or differential stress before fracture growth and coalescence triggers macroscopic failure (e.g., Bieniawski, 1968; Brace, 1964; Brace et al., 1966; Paterson and Wong, 2005, p. 111). Previous analyses have attributed this quasistatic growth to the propagation of wing cracks from inclined shear cracks because the stress intensity factor at an isolated wing crack tip may decrease as it propagates away from the stress concentration at the tip of the inclined shear crack, particularly if the fracture propagates into a region with some lateral compression (Brace and Bombolakis, 1963; Brace et al., 1966; Fairhurst and Cook, 1966; Ashby and Sammis, 1990; Horii and Nemat-Nasser, 1985; Paterson and Wong, 2005 p. 120). This decrease of the stress

* Corresponding author.
E-mail address: j.a.mcbeck@geo.uio.no (J. McBeck).

https://doi.org/10.1016/j.tecto.2023.230191
Received 25 March 2023; Received in revised form 19 December 2023; Accepted 20 December 2023
Available online 24 December 2023

intensity factor then stabilizes growth and allows strain-hardening before macroscopic, catastrophic failure. However, wing crack growth may only stabilize when the fractures are relatively isolated, and not when neighboring cracks begin to perturb each other's local stress field. Moreover, such idealized wing crack development from preexisting inclined shear cracks is rarely observed in experiments on natural, three-dimensional rocks (e.g., Renard et al., 2019a, 2019b; Cartwright-Taylor et al., 2020; McBeck et al., 2021a, 2023a).

Because fracture opening appears to precede some, but not all, earthquakes (e.g., Chiarabba et al., 2020), constraining fracture characteristics that help predict the timing of catastrophic failure in triaxial compression experiments, such as length and orientation, may help forecast the timing of large earthquakes in the crust. In particular, geophysical observations and laboratory experiments suggest that monitoring the volume of fractures in the crust, through changes in the seismic wave speeds and anisotropies, could help forecast the timing of large earthquakes (e.g., Chiarabba et al., 2020; Shreedharan et al., 2021a, 2021b). However, the associated changes in seismic wave properties have only been observed preceding some earthquakes (Bakun et al., 2005). This lack of detection may be due to the competing effects of fracture opening near the crustal slip zone, and the closure of fractures in the surrounding wall rock (Shreedharan et al., 2021b).

Another characteristic of deformation that may be useful for forecasting efforts is the evolving spatial organization of deformation, such as seismicity and fractures. Geophysical observations in Southern and Baja California reveal that the localization of low magnitude seismicity preceded the main shocks of the $M > 71{,}992$ Landers, 1999 Hector Mine, 2010 El Mayor-Cucapah, and 2019 Ridgecrest earthquakes (Ben-Zion and Zaliapin, 2020). The seismicity generally increased in localization in the final two to three years preceding the main shock. However, for short time periods during this general increase, localization remained at similar values or decreased, that is, delocalized. Consistent with these trends, monitoring the spatial organization of the high magnitudes of shear and dilative strain, and fractures in X-ray tomography triaxial compression experiments with increasing differential stress reveals phases of delocalization within a broader trend of increasing localization as the rocks approach macroscopic failure (McBeck et al., 2021a, 2022b) (e.g., Fig. 1b). Bifurcation theory (Rudnicki and Rice, 1975) and visco-elastic damage rheology models (Lyakhovsky et al., 2011) have explicitly linked the onset of macroscopic failure in rocks to the localization of strain. Moreover, experiments that track the location of acoustic emissions under triaxial compression find that following the peak stress, acoustic emissions can localize into an elongate zone that appears to produce the macroscopic, system-spanning shear fracture identified post-mortem (Lockner et al., 1991; Aben et al., 2019). A few recent experiments also reveal evidence of localization preceding failure on preexisting faults (Dresen et al., 2020; Bolton et al., 2023; Marty et al., 2023). Much previous work has recognized the importance of localization in the macroscopic failure of rocks and heterogeneous materials (e.g., Satoh et al., 1996; Benson et al., 2007; Rizzo et al., 2017), but few analyses have focused on the temporary decreases in localization, or attempted to identify the factors that promote these episodes of delocalization. Identifying these factors may help earthquake forecasting efforts that use the evolving spatial distribution of seismicity to recognize the precursory phase leading to large earthquakes.

In this work, we use a suite of six X-ray tomography triaxial compression experiments with systematically varying confining stress, fluid pressure, and amount of preexisting damage to identify the fracture characteristics that control localization and delocalization, and the characteristics that control the timing of macroscopic, catastrophic failure. We develop machine learning models to predict three targets. One set of models predicts the stress distance to macroscopic failure, $\Delta\sigma$, from the differential stress acting on the rock when an X-ray tomogram was acquired, σ_D, and the differential stress at macroscopic failure, σ_D^F, $\Delta\sigma = \left(\sigma_D^F - \sigma_D\right)/\sigma_D^F$ (Fig. 1a). The second set of models predicts the

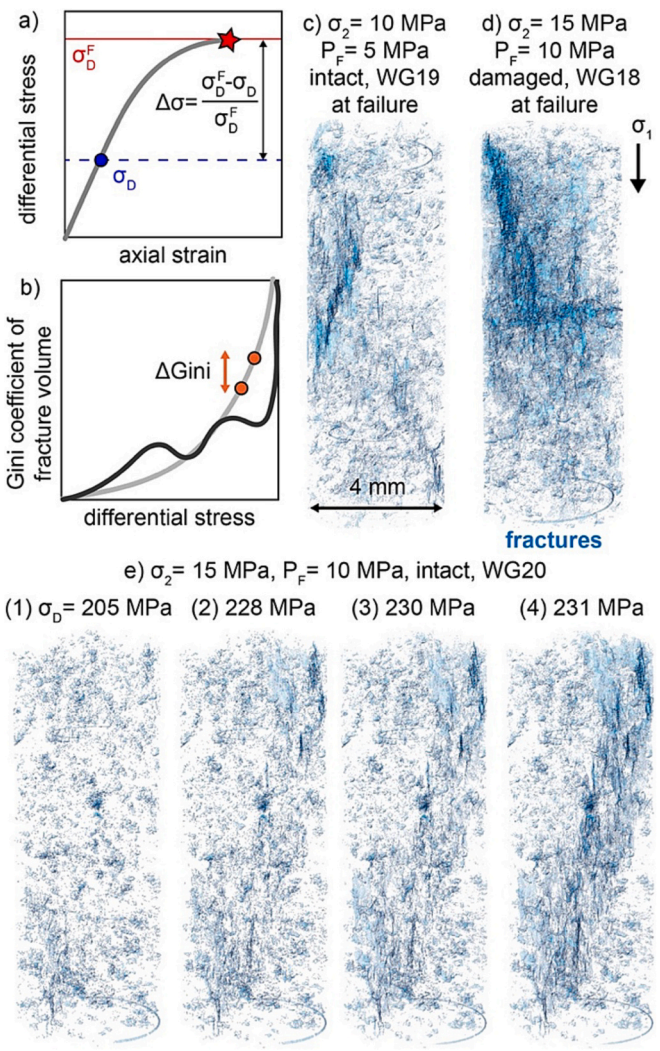

Fig. 1. Sketch of the predictions of the machine learning models: a) the stress distance to failure, $\Delta\sigma$, b) the Gini coefficient calculated from the volume of the fractures at each differential stress step in the triaxial compression experiments, and the change in the Gini coefficient from one stress step to the next, ΔGini. c–d) Three-dimensional representations of fractures identified in the final tomogram acquired immediately preceding macroscopic failure in two experiments with confining stresses, σ_2, of 10 MPa and 15 MPa, fluid pressures, P_F, of 5 MPa and 10 MPa, with nominally intact and heat-treated (damaged) Westerly granite. The fractures are shown with slightly transparent blue objects, and the different shades of blue correspond to different densities of fractures. e) Fractures at four differential stress steps in one experiment with σ_2=15 MPa and P_F=10 MPa on intact rock. Tomogram (#4) was the final tomogram acquired preceding macroscopic failure. The circular shapes at the bottom of the images are ring artefacts and excluded from the analysis. (For interpretation of the references to colour in this figure legend, the reader is referred to the web version of this article.)

localization of the fracture networks using the Gini coefficient of the fracture volume, which measures the deviation of a population from uniformity, and the third set predicts the change in the Gini coefficient from one stress step to the next (Fig. 1b). Larger values of the Gini coefficient indicate more unequal distributions (Gini, 1921) with a few larger fractures and many smaller fractures, while smaller values indicate a more uniform distribution with fractures of the same or similar volumes. Previous analyses show that the Gini coefficient can continually increase and accelerate toward failure in triaxial compression experiments (e.g., Fig. 1b) (McBeck et al., 2021a). The coalescence of many small fractures into larger fractures is likely the dominant form of

fracture development that produces the increase in the Gini coefficient. In other experiments, the Gini coefficient may generally increase, but also temporarily decrease, producing phases of delocalization toward macroscopic failure, and thus non-monotonic behavior. Identifying the factors that promote these phases of delocalization may improve efforts to forecast the timing of catastrophic failure.

In order to identify the characteristics that control localization and delocalization, and that control the timing of failure, we identify the characteristics that produce the best model predictions of each of the three targets. To compare the influence of the different confining stress, fluid pressure, and preexisting damage on the predictability of failure and localization, we develop models using data from each individual experiment, as well as models using data from all the experiments combined. Previous work suggests that varying amounts of preexisting damage may produce different modes of catastrophic failure. In particular, higher levels of preexisting damage could promote more continuous and gradual transitions to failure, whereas less preexisting damage could promote more abrupt transitions (e.g., Tang et al., 2000; Vasseur et al., 2015; Cartwright-Taylor et al., 2020). Consequently, the amount of preexisting damage may influence the timing of the precursory phase leading to macroscopic failure, and thus the predictability of failure. To assess the ability to upscale the results to crustal fault networks, we vary the volume of the system used to extract the fracture characteristics and compare the resulting sets of characteristics identified as important in the different models.

In previous studies we used fracture characteristics identified in a different set of X-ray tomography experiments to predict the stress distance to failure (McBeck et al., 2020), and to predict the value of fracture characteristics using other characteristics (McBeck et al., 2022a). However, these analyses did not include the Gini coefficient of the fracture volume, and so did not reveal insights into the ability of this localization metric to help predict the timing of macroscopic failure, or insights into the factors that control delocalization. Another previous analysis attributed differences in the localization of fracture networks to varying confining stresses and grain sizes of minerals in crystalline rock (McBeck et al., 2021a). However, this previous work did not have access to the new experiments with systematically varying confining stress, fluid pressure and damage, and so was not able to robustly compare these effects. The present analysis will compare these influences.

2. Methods

2.1. Triaxial compression X-ray tomography experiments

We performed six triaxial compression experiments at beamline ID19 at the European Synchrotron Radiation Facility, in Grenoble, France. We used 10 mm tall and 4 mm diameter cylinders of Westerly granite. Westerly granite is a low-porosity crystalline rock dominated by interlocking quartz, feldspar, and biotite. Westerly granite has a mean grain size of 0.75 mm and an initial porosity of <1% (e.g., Atkinson and Meredith, 1987).

Using the Hades triaxial compression apparatus (Renard et al., 2016), we imposed a constant confining stress in each experiment in the range 5–20 MPa, and constant pore fluid pressure in the range 0–10 MPa (Table S1). We varied the confining stress and fluid pressure so that five of the six experiments experienced the same effective stress, confining stress minus fluid pressure (P_e=5 MPa), and the remaining experiment experienced P_e=10 MPa. Consequently, this suite of experiments does not allow differentiating between the influence of pore fluid pressure and confining stress. We then increased the axial stress, σ_1, in steps of 0.5–5 MPa, with smaller steps closer to failure, until the rock failed with a stress drop. After each step increase in σ_1, we acquired an X-ray tomogram in under 1.5 min while the rock was inside the Hades apparatus and thus under constant loading.

To assess the influence of preexisting damage on the timing of macroscopic failure and localization of the fracture networks, we deformed intact and heat-treated (damaged) Westerly granite samples drilled from the same block. We damaged the cores by heating them in an oven with an initial heating rate of 4 °C/min from room temperature to 650 °C, and then for five hours at 650 °C, and then with a cooling rate of 4 °C/min to room temperature. This heating procedure causes the damaged rock cores to fail at lower differential stresses than the intact rock cores for the same confining stress and effective stress conditions (Fig. S1). We performed all the experiments at ambient room temperature in the range 22–24 °C. For the experiments that include fluid pressure, we saturated the granite cores in deionized water in a vacuum chamber for two weeks preceding the experiment.

Following each experiment, we reconstructed the radiographs into three-dimensional volumes. The volumes are 1600x1600x1600 voxels, and each voxel side length is 6.5 μm. During reconstruction, we applied methods to remove acquisition noise, such as ring artefacts. We reduced the remaining noise in the reconstructed, three-dimensional data using the software Avizo3D™, including the application of a non-local means filter (Buades et al., 2005). After these steps, the data contain some visible noise, such as a few ring artefacts. Later, we apply additional post-processing techniques to exclude these artefacts from the analyses, which we describe below. We segmented the solid rock from the fractures using a method similar to Otsu's thresholding technique to identify a global threshold between the solid material and the fractures (McBeck et al., 2021c). This method produces segmented tomograms with porosity similar to values measured in the laboratory with sample imbibition when the pores have dimensions above the spatial resolution of the tomograms, which is in the range 2–3 voxels (Renard et al., 2019a). We then applied several processing steps to the segmented tomograms in Avizo3D™, including Label Analysis, that identify individual fractures using connected clusters of voxels, and calculate the geometric characteristics of fractures.

We calculated the macroscopic axial strain done on the rock cores, ε_{zz}, by identifying the height of the rock core in each tomogram. Consequently, the spatial resolution and quality of the tomogram influences the calculated ε_{zz}. An alternative method of constraining the axial strain uses the displacement recorded by the linear variable displacement transducer (LVDT) installed on the deformation apparatus. However, the LVDT displacement incorporates the deformation of the rock as well as the elastic response of the apparatus. Consequently, the axial strain derived from the tomograms is more representative of the deformation of the rock core than the strain derived from the LVDT. The axial strain calculated from the tomograms is similar to the displacement recorded by the LVDT after correcting for the elastic deformation of the rig (Fig. S2), lending confidence to the ε_{zz} calculated from the tomograms.

Following previous work that characterizes or predicts the distance to failure using the stress (e.g., Renard et al., 2018; Kandula et al., 2019; McBeck et al., 2020), we predict the distance to failure in terms of the differential stress. Consequently, the calculated ε_{zz} does not influence the key results of the analysis because we use the characteristics of the fracture networks to predict the stress distance to failure. To predict the Gini coefficient and ΔGini, we use the characteristics of the fracture networks as well as the macroscopic σ_D and ε_{zz}. Later, we show that some of the models developed for individual experiments use ε_{zz} to predict the Gini coefficient (Section 3.2). This result lends confidence to the ε_{zz} calculated from the tomograms.

2.2. Machine learning models

Here, we use machine learning to identify the characteristics of fracture networks that are the most useful for predicting the timing of catastrophic failure, the localization, and the changes in localization. As described above, we develop the models to use geometric characteristics of the fracture networks revealed in the X-ray tomograms to predict 1) the stress distance to failure, 2) the Gini coefficient at a given stress (or time) step, and 3) the change in the Gini coefficient, ΔGini, from one

stress step to the next. The Gini coefficient uses the Lorenz curve to measure the deviation from a uniform distribution (e.g., Gini, 1921). The Lorenz curve shows the proportion of the total amount of a population, such as fracture volume, that is included in the bottom percentile of a population. The Gini coefficient is one minus twice the integral of the Lorenz curve. Consequently, larger Gini coefficients indicate that the total volume of the fractures in a network is dominated by a few fractures, whereas lower Gini coefficients indicate that the total volume is more equally distributed among all the fractures.

The processing steps described in Section 2.1 produce a suite of characteristics for each individual fracture in each stress step, including the volume of the fracture, the centroid of the fracture, the surface area of the fracture, the eigenvalues of the fracture, and the orientation of each eigenvector relative to the vertical axis, parallel to the σ_1 direction, and one of the horizontal axes, parallel to the σ_2 direction (Table S2). The eigenvalues and eigenvectors of each fracture are calculated from the covariance matrix of the voxels of the fracture. We characterize the length of the fractures using the first eigenvalue, and the apertures of the fractures using the second and third eigenvalues. We also use ratios between eigenvalues to define the anisotropy (1-third eigenvalue/first eigenvalue), elongation (second eigenvalue/first eigenvalue), and flatness (third eigenvalue/s eigenvalue).

To test the influence of system size on the factors that control the timing of failure and localization, we provide features to the model that represent characteristics of the population of fractures within one or more subvolumes at each stress step (and tomogram). In particular, the data table fed to the models have rows that represent each subvolume at each stress step. When the length of one side of the subvolume is larger than the height of the rock core (subvolume size, s=1600 voxels, or about one centimeter), then the data table of each experiment has one row for each stress step. We test subvolume sizes of 600 voxels (3.9 mm) and 400 voxels (2.6 mm), which produce two and three subvolumes at each differential stress step, respectively. We use a mask to remove the upper and lower pistons, and the jacket that encases the rock core from the images, so only the fractures identified within the rocks are used in the analysis.

For a given subvolume size, we identify all the fractures within the subvolume at a particular stress step using the centroid of the fractures. We then calculate statistics of each geometric characteristic of all the fractures within the subvolume, such as the volume. These statistics are the mean, standard deviation, maximum, and several percentile values (25th, 50th, 75th, 90th). We include features that describe the confining stress and fluid pressure of the experiment (with the numbers prescribed in each experiment), as well as whether the rock is damaged or not (with a one or zero). For the models that predict the Gini coefficient and change in the Gini coefficient, we include features that describe the macroscopic time within the experiment, including the cumulative axial strain, ε_{zz}, and the differential stress, σ_D. For these models, we exclude the features that describe the fracture volume because the Gini coefficient is calculated from the fracture volume. Table S2 lists all 115 features used in the present study.

In addition to the influence of the subvolume size, s, we also test the influence of excluding relatively thicker or more tortuous fractures and voids by varying the minimum shape anisotropy, a, from 0.25 to 0.75, and the minimum volume of individual fractures, v, from 100 to 1000 voxels. We show the results of varying s and v in the main manuscript because varying these parameters may provide insights into the most appropriate methods of analyzing crustal fault networks. Removing voids with lower anisotropies in the experimental analysis, in contrast, is motivated by removing artefacts of the tomogram acquisition and segmentation, such as the few ring artefacts that remain after filtering the data (e.g., at the bottom of the core in Fig. 1d).

To predict the change in the Gini coefficient, we calculate the Gini coefficient within each subvolume at each differential stress step, for a given set of s, v, and a for each experiment. We then apply a median filter with a window size of five data points in order to smooth small perturbations in the curve of the Gini coefficient and differential stress for each subvolume size. We calculate the change in the Gini coefficient from one scan to the next, ΔGini, using this smoothed curve. We also tried to predict ΔGini without smoothing the data and achieved similar results to those shown here. We tested predicting the ΔGini divided by the change in ε_{zz}, and ΔGini divided by the change in σ_D from one scan to the next. The performance of the models that predict ΔGini are the same as the models that predict $\Delta\text{Gini}/\Delta\varepsilon_{zz}$ and $\Delta\text{Gini}/\Delta\sigma_D$, and so we only show the results of predicting ΔGini.

We develop XGBoost regression models in this work. This method is a widely used algorithm in machine learning (e.g., Rouet-Leduc et al., 2017; Hulbert et al., 2019; Shreedharan et al., 2021a) that we have used in previous analyses (e.g., McBeck et al., 2020, 2022a). We estimate the influence of the features on the model predictions using Shapely Additive Explanations (SHAP), a widely used metric in machine learning (Lundberg and Lee, 2017; Pedregosa et al., 2011). We report and compare the mean absolute value of the SHAP (mean |SHAP|) of each feature calculated from the SHAP values of all the data points (e.g., samples) provided to the models.

We develop models using data from individual experiments, as well as all of the experiments combined together. We separate the training (70%) and testing (remaining 30%) datasets so that there is no overlap between these two sets. For the datasets with the largest tested subvolumes, s =1600 voxels, each sample is distinct in time (stress step) and space. For the datasets with smaller subvolumes, s=400 voxels and 600 voxels, each stress step includes three and two subvolumes, respectively. We randomize the times that occur in the training and testing datasets such that times earlier and later in the experiment can occur in either dataset. Comparing the performance of models developed with this randomized splitting and models developed from training and testing data that are continuous in time does not produce significant differences in the model performance.

For each set of targets, experiments, and parameters of s, v, and a, we develop ten unique models that differ only in the separation of the training and testing datasets. We develop these models to reduce the influence of random variations in the training and testing dataset on the model performance. We then report the mean ± one standard deviation of the R^2 values in the results. Because we develop these ten models for each set of parameters, we have ten sets of SHAP values for each of these combinations. To simplify the identification of the features that have the strongest influence on the model performance, we weight each SHAP value by the R^2 value of the model, and then average these weighted values for the models with R^2>0.7 for predicting the distance to failure and the Gini coefficient, and with R^2>0.6 for predicting the ΔGini (e.g., McBeck et al., 2020, 2022a). To further compare the influence of each feature on the predictions, after we examine the R^2-weighted SHAP values, we develop models that only include particular subsets of features. Comparing the performance of models developed with only subsets of features provides a more robust method of assessing the influence of each fracture characteristic on the model predictions than comparing the SHAP values.

3. Results

3.1. Macroscopic mechanical behavior

Here, we focus on models that predict the stress distance to macroscopic failure, $\Delta\sigma = \left(\sigma_D^F - \sigma_D\right)/\sigma_D^F$. Fig. 2 shows the axial strain and differential stress when a tomogram was acquired in each experiment. Many of the experiments produce non-linear stress-strain behavior early in loading because the rock core was not completely in contact with the pistons of the apparatus at the beginning of the experiment, and because some small preexisting fractures or voids closed (Fig. 2). Several of the experiments host an extended phase of yielding preceding macroscopic failure in which the slope of the axial strain-differential stress curve

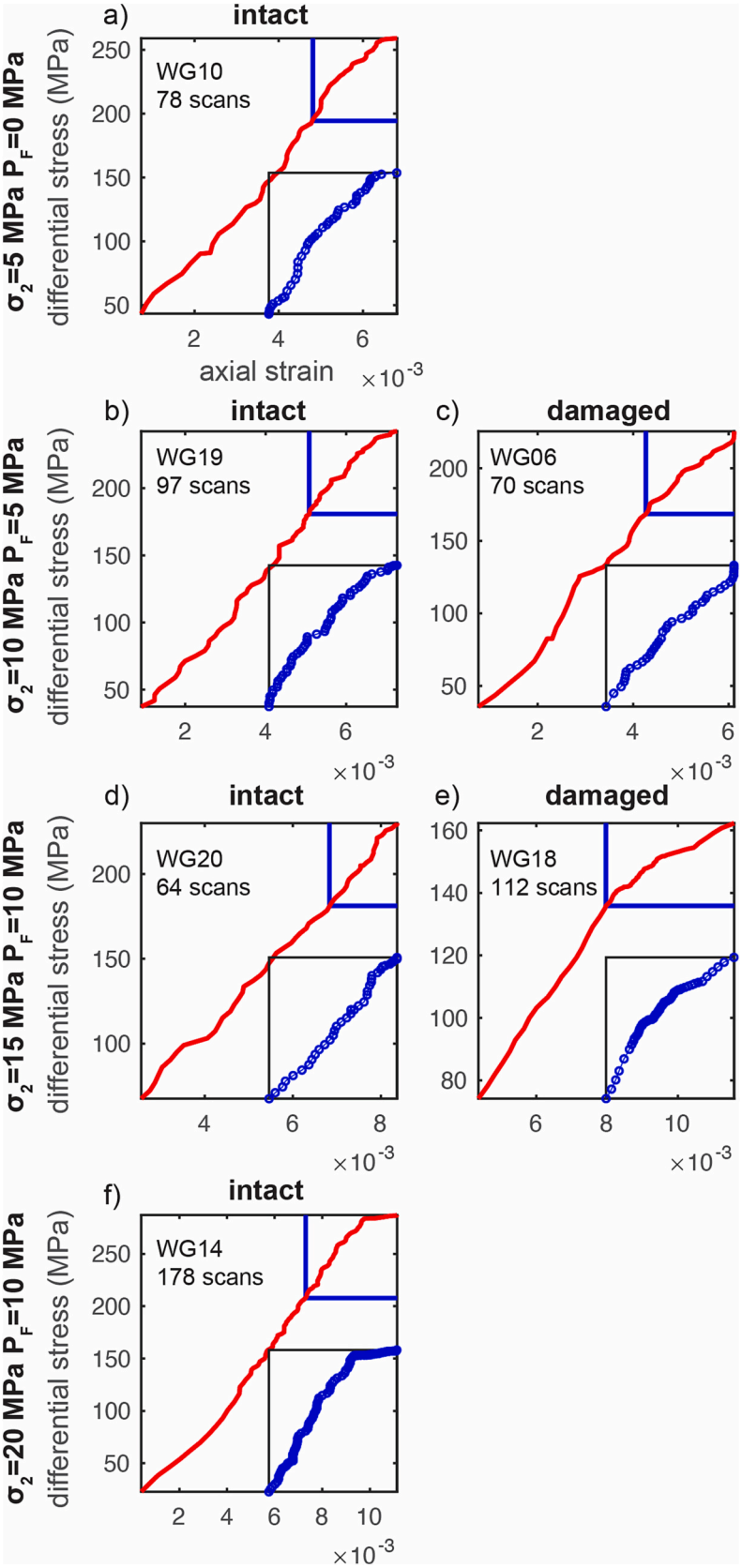

Fig. 2. Axial strain and differential stress conditions when each tomogram was acquired in the six experiments. The applied confining stress, σ_2, and fluid pressure, P_F, are listed to the left of each set of plots. The data shown with the blue circles in the insets are the portion of the experiment within 70% of the differential stress at macroscopic failure, highlighted with blue rectangles. The number of scans acquired in each experiment is listed in each plot. (For interpretation of the references to colour in this figure legend, the reader is referred to the web version of this article.)

decreases toward nearly zero (WG20, WG18, WG14). These experiments tend to have higher confining stresses (15 MPa and 20 MPa) than the experiments that do not produce this behavior (5 MPa and 10 MPa). The experimental design may not have captured the yielding phase preceding failure in the experiments with lower confining stress because the final differential stress step increase of 0.5 MPa was too large to allow a prolonged phase of yielding. However, the mechanical behavior observed here is consistent with previous experiments that observe a longer yielding phase, in terms of the accumulated axial strain, for rocks deformed at higher confining stresses than lower confining stresses (e.g., Paterson, 1958; Paterson and Wong, 2005 p. 212).

3.2. Predicting the distance to macroscopic failure

The models use the characteristics of the fracture networks to predict the distance to failure. Consequently, we vary the populations of fractures included in the models to assess 1) how the volume or size of the fractures controls the predictability of failure, and 2) how the size of the system controls the predictability of failure. We exclude fractures with volumes smaller than particular volume thresholds, v, of 100 to 1000 voxels. We also vary the size of the subvolume, s, used to calculate the statistics of the fracture characteristics from the height of the tomogram (s=1600 voxels), to about half (s=600 voxels), and one third (s=400 voxels) of the height of the tomogram. We develop models for individual experiments and all the experiments combined to assess differences in predictability due to the varying confining stress, fluid pressure, and initial damage of each rock.

The R^2 values are above 0.9 for all of these models, indicating that the models can predict $\Delta\sigma$ with strong correlations between the predicted and observed $\Delta\sigma$ (Fig. 3). This performance is a significant improvement beyond previous efforts to predict the timing of macroscopic failure using characteristics of the fracture networks, which only achieved R^2 values of about 0.6 (McBeck et al., 2020).

Varying v does not systematically alter the R^2 values for the model that uses data from all the experiments, or the models developed from individual experiments (Fig. 3a). Varying s has a stronger influence on the R^2 value than varying v (Fig. 3b). Increasing s from about the radius of the base of the rock cylinder (400 voxels) to the height of the rock cylinder (1600 voxels) increases the R^2 value from about 0.8 to above 0.95 for each experiment and combination of experiments. Providing less data (i.e., a lower number of subvolumes) to the models thus produces higher R^2 values. Generally, one may expect that providing more data to a machine learning model produces better model performance. However, the quality of the data can influence whether the model performance decreases or increases. In the Discussion section, we describe how the heterogeneity of the fracture networks allow the models to perform better when they have access to a lower number of larger subvolumes, rather than a higher number of smaller subvolumes.

To identify which fracture characteristics control the model predictions, and thus may be beneficial for forecasting the timing of catastrophic failure, we first identify the features with the highest mean |SHAP| values for the sets of the models. Table S3 shows the features with the R^2-weighted mean |SHAP| values >50% of the maximum of these values for each experiment, and combination of experiments, with varying s. These values approximate the influence of each feature on the model results, and thus indicate which features the models rely or depend on. All models developed from individual experiments with s=1600 voxels, except experiment WG19, rely on the Gini coefficient of the fracture volume to predict the timing of failure. When the models use data from all the experiments and s=1600 voxels, they rely on the mean of the first eigenvalue, proportional to the length of the fracture. For smaller s, the individual experiment models and the combined experiment model rely on the shape anisotropy, surface area, and eigenvalues of the fractures. Consequently, varying the size of the system used to calculate the statistics of the fracture properties, the Gini coefficient, and other features changes the features that control the model predictions, according to the SHAP values.

To better quantify the influence of each fracture characteristic on the predictions, we develop models using subsets of features (Fig. 4). The performance of the models developed with different subsets of features is likely a more reliable measure of the relative usefulness of each characteristic to the predictions than the SHAP values. The models include features derived from individual fracture characteristics (Fig. 4b, d, f), and from a combination of characteristics that include the most important feature identified using the SHAP values (Table S3), the first eigenvalue (Fig. 4a, c, e). We focus on models that use data from all the experiments because they may be more representative of the fundamental processes in crystalline rock than models developed from individual experiments.

When the models are developed with individual characteristics, the localization metrics, the Gini coefficient and the distance between fractures, produce relatively poorly performing models. These models

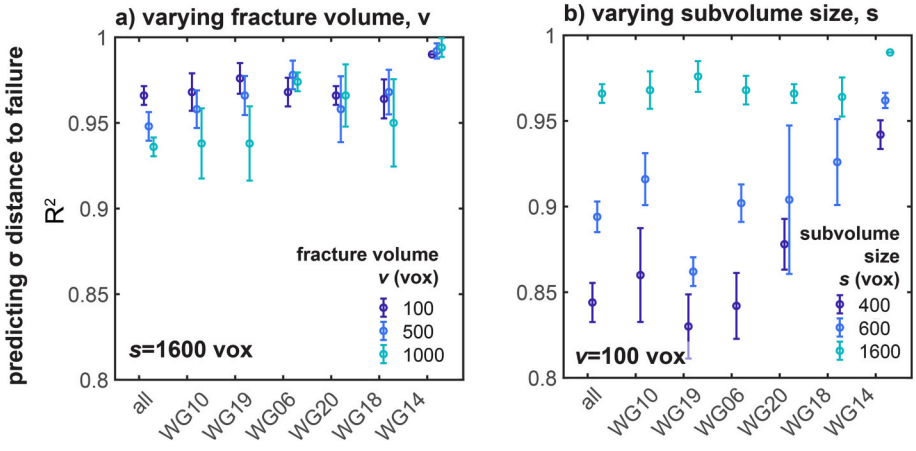

Fig. 3. Performance, R^2, of models that predict the stress distance to failure, $\Delta\sigma$, for all of the experiments combined together and the individual experiments. The plots show the results using a) different thresholds of the minimum fracture volume included in the data, v, and b) different subvolume sizes to extract the data, s. The horizontal axes list the individual experiment or combination of all of the experiments (all) used to develop the model, and the applied confining stress, σ_2, of the individual experiments. The model performance is reported as the mean ± one standard deviation of the R^2 values of models developed with different training and testing datasets for each individual experiment and all of the experiments. The data provided to the models shown in (a) have s=1600 voxels, or one subvolume per differential stress step. The data provided to the models shown in (b) include fractures with v>100 voxels. Increasing v both increases and decreases the model performance, depending on the experiment (a). Increasing s increases the model performance (b).

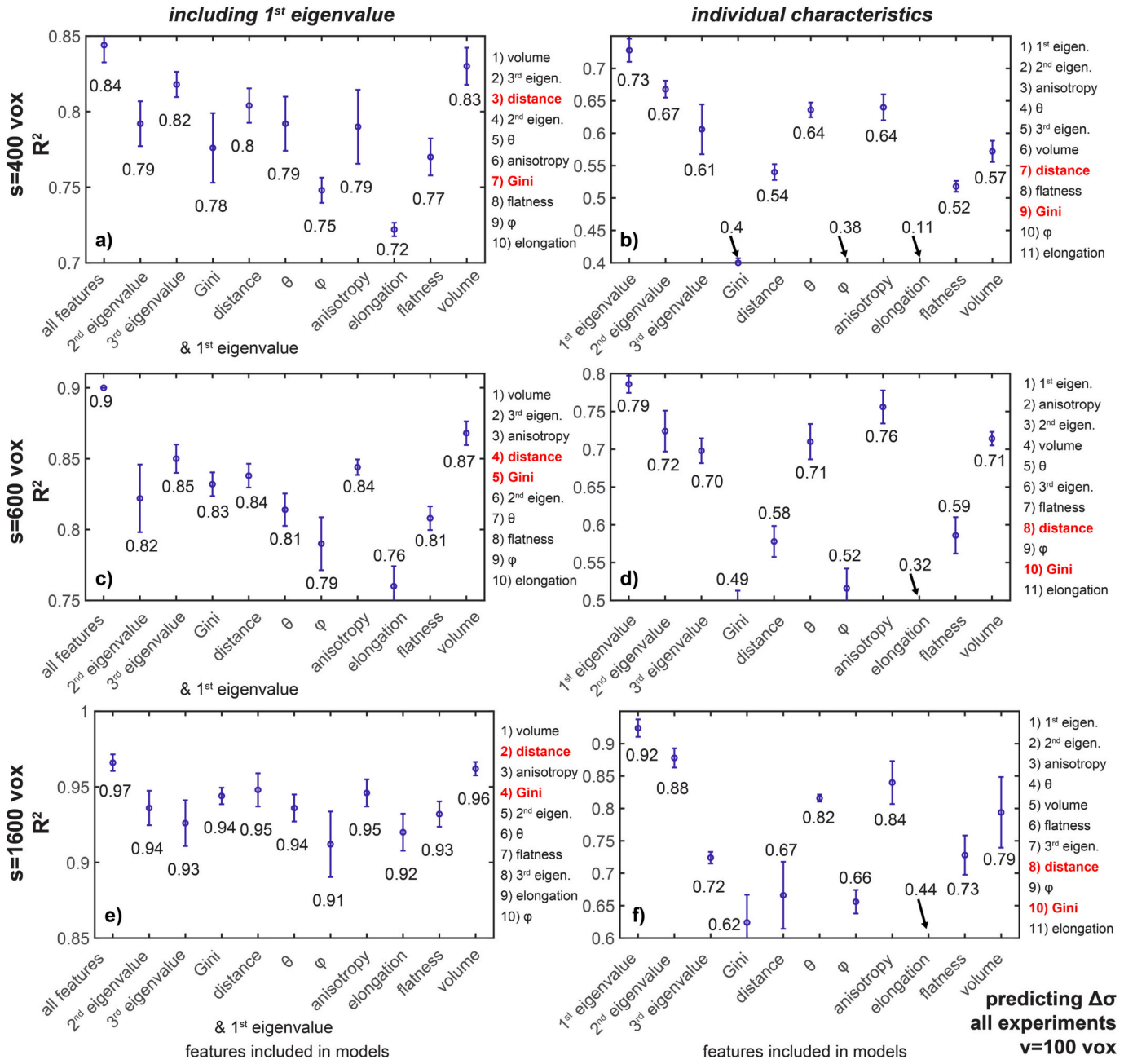

Fig. 4. Performance of models that predict $\Delta\sigma$ using subsets of features with data from all the experiments for v=100 voxels and varying subvolume size: a–b) s=400 voxels, c–d) s=600 voxels, and e–f) s=1600 voxels. The left column (a, c, e) shows the results of models that use a combination of features that include the first eigenvalue (i.e., the fracture length). The right column (b, d, f) shows the results of models that use individual characteristics as features, such as the fracture anisotropy or distance between fractures. The model performance is reported as the mean ± one standard deviation of the R^2 values of models developed with different training and testing datasets. The text next to each data point is the mean R^2 value. The list of characteristics to the right of each plot shows the ranking of the model performances, where number one is the best performing model. Models developed with features that describe the spatial localization, including the distance between fractures and the Gini coefficient of the fracture volume, are highlighted with bold, red font. When the models are developed with individual characteristics, the localization metrics produce relatively poorly performing models. When the models are developed with combinations of characteristics that include the first eigenvalue, the localization metrics and particularly the distance between fractures produce models that perform better than the majority of the models developed with the other features. (For interpretation of the references to colour in this figure legend, the reader is referred to the web version of this article.)

rank from the seventh to tenth best-performing models out of eleven, depending on the subvolume size (Fig. 4). When the models are developed with combinations of characteristics that include the first eigenvalue, the models that use the first eigenvalue and the localization metrics perform better than the majority of the other models. The models developed with the distance between fractures and the first eigenvalue rank from the second (s=1600 voxels) to the fourth (s=600 voxels) best-performing models out of eleven. The models developed with the Gini coefficient and the first eigenvalue rank from the fourth (s=1600 voxels) to the seventh (s=400 voxels) best-performing models. Other than the localization metrics, the characteristics that produce the best performing models when they are combined with the first eigenvalue include the volume and anisotropy of the fractures.

In summary, characterizing the length of the fractures, with the first eigenvalue, provides more useful information about the distance to macroscopic failure than the other tested characteristics, including the

anisotropy, the orientation relative to the σ_1 direction, θ, and the localization metrics. When the fracture length is combined with the other fracture network properties to predict the distance to failure, the volume, anisotropy, distance between fractures, and for some subvolume sizes, the Gini coefficient, provide more useful information than the other tested characteristics.

Varying the subvolume size does not significantly change the key observations. For the models developed with the individual characteristics, the first and second eigenvalues and the anisotropy produce the three best-performing models for all of the subvolume sizes. The volume of the fractures and θ produce the fourth to sixth best-performing models. Finally, the distance between fractures and the Gini coefficient produce the seventh to tenth best-performing models, and the elongation produces the worst-performing models.

For models developed with combinations of characteristics that include the first eigenvalue, the volume produces the best-performing models for all the subvolume sizes. The elongation, flatness and orientation relative to the σ_2 direction, φ, produce the worst-performing models. For the smaller subvolume sizes, s=400 voxels and 600 voxels, the third eigenvalue produces the second best-performing model, and the distance between fractures produces the third or fourth best-performing model. When s=1600 voxels, the distance produces the second best-performing model, and the Gini coefficient produces the fourth best-performing model. Consequently, increasing the subvolume size increases the usefulness of the localization metrics, and particularly the usefulness of the Gini coefficient, for predicting the distance to failure.

3.3. Predicting localization: The Gini coefficient

Next, we develop models to predict the Gini coefficient of the fracture volume using characteristics of the fracture networks. The Gini coefficient increases toward failure in all of the experiments (Fig. 5). In half of the experiments (WG10, WG06, WG14), the Gini coefficient temporarily decreases, producing episodes of delocalization. Previous analyses attribute phases of delocalization to the presence of heterogeneities and stress shadows (e.g., McBeck et al., 2021a, 2021b). Consequently, one would expect the damaged (heat-treated) rock cores to favor episodes of delocalization rather than the nominally intact rocks. However, this suite of experiments shows that the intact rocks can also experience phases of delocalization, and that damaged rocks can host increasingly localized fracture networks without phases of delocalization. Due to this behavior, we develop models to predict the Gini coefficient at particular stress steps, and the change in the Gini coefficient between stress steps.

Similar to the set of models that predict the distance to failure, we test the influence of varying the fracture volume and subvolume size on the models that predict the Gini coefficient. Varying v does not produce systematic difference in the model performance (Fig. 6a), similar to the models that predict the distance to failure (Fig. 3). Increasing s tends to decrease the R^2 values for all but the experiment WG14 models (Fig. 6b), in contrast to the models that predict the distance to failure (Fig. 3). Varying both of these parameters produces only small changes in R^2 values as all of the mean R^2 values are above 0.90.

To identify the fracture characteristics that control the model predictions, and thus the Gini coefficient, we examine the sets of features with the highest mean |SHAP| values, similar to the previous section. All of the models developed from individual experiments with s=1600 voxels, rely on the macroscopic axial strain, ε_{zz}, or the macroscopic differential stress, σ_D (Table S4). When all the experiments are combined (Table S4), and s=1600 voxels, the models primarily rely on the standard deviation of the second eigenvalue, which is proportional to the larger of the two apertures of the fracture. For the smaller s, the models depend on the surface area of the fractures and the first or second eigenvalues. Consequently, changing the system size changes the fracture characteristics and macroscopic parameters that are useful for estimating the Gini coefficient for models developed for individual experiments, according to the SHAP values.

We next develop models using subsets of features to more robustly quantify the influence of each characteristic on the model performance (Fig. 7). We focus on models developed using data from all experiments. The key difference between the performance of models developed with

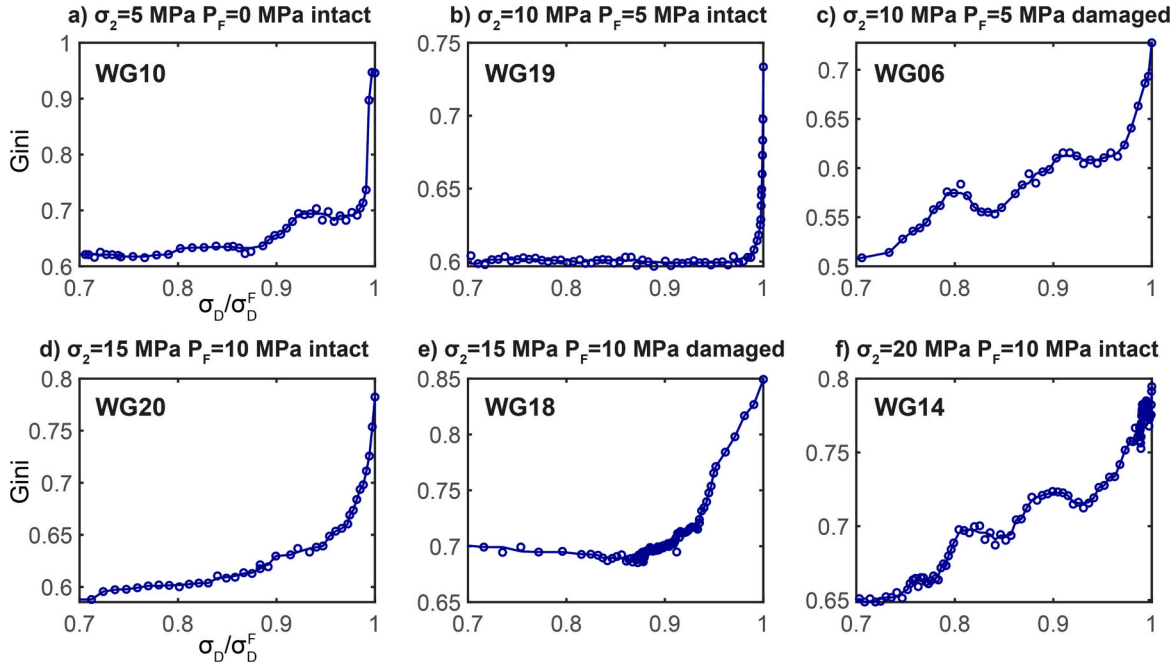

Fig. 5. The Gini coefficient calculated from the volume of the fractures at each tomogram as a function of the σ_D/σ_D^F for each experiment using the whole tomogram. Some experiments include phases in which the Gini coefficient decreases, indicative of temporary episodes of delocalization (a, c, f), while others host a continual increase of localization. The curves are median filters through the data, which are used to calculate the change in the Gini coefficient, as described in the Methods section.

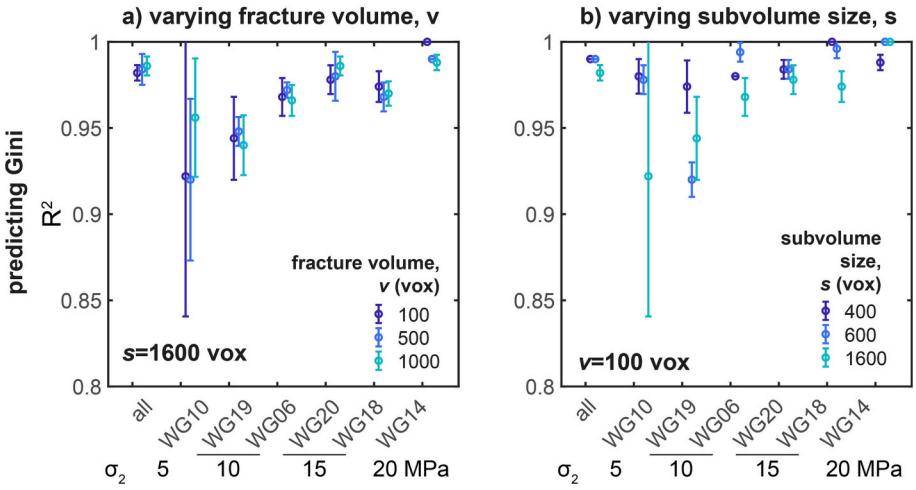

Fig. 6. Performance of models that predict the Gini coefficient with varying minimum fracture volume, v (a), and subvolume size, s (b). The model performance is reported as the mean ± one standard deviation of the R^2 values of models developed with different training and testing datasets. Increasing s produces worse model performances.

the different subvolume sizes is that when s=1600 voxels, models that only use the features that describe the time in the experiment, such as ε_{zz} and σ_D, produce high R^2 values (0.96). In contrast, for the smaller subvolumes, these models perform poorly with R^2 values of 0.03 and 0.09.

Except for models developed with the time-based features, the relative performance of the models is similar for the different subvolume sizes. When s=400 voxels, the subsets of features that produce the best-performing models are the 1) surface area, 2) eigenvalues, and 3) distance between fractures. These subsets of features produce the best performing models when s=600 voxels, as well as features derived from the orientation of the fractures relative to the σ_1 direction, θ. When s=1600 voxels, the subsets of features that produce the best-performing models are those identified when s=600 voxels, as well as the time-based features (ε_{zz} and σ_D), and the anisotropy. The elongation and flatness produce some of the worst performing models for all the subvolume sizes.

3.4. *Predicting the change in localization: ΔGini*

We now focus on models that predict the change in the Gini coefficient, ΔGini (Fig. 8). Varying the parameters v and s does not produce systematic trends in the model performance. For some combinations of these parameters and some experiments (WG19, WG20, WG18), the models perform with moderate to strong correlations between the predicted and observed ΔGini. These experiments host the most systematic evolutions of the Gini coefficient, and do not contain phases of delocalization (Fig. 5). The poor performance of models that predict ΔGini for experiments with phases of delocalization reveals the difficulty of predicting these temporary episodes. Examining the features that most strongly control the predictions for models with R^2 values >0.6 (Table S5) shows that the ε_{zz} and σ_D are the most important features for models developed with s=1600 voxels. For the smaller subvolumes, the eigenvalues and flatness are the most important features.

4. Discussion

4.1. *Predictability of the stress distance to macroscopic failure*

To assess how localization is linked to the macroscopic failure of crystalline rocks in the upper crust, we developed machine learning models to predict the stress distance to catastrophic failure using characteristics of the fracture networks. These models perform with R^2 values of 0.8–0.95, and thus better than previous analyses that predicted the stress distance to failure in crystalline rocks with R^2 values of about 0.6 (McBeck et al., 2020). The present models may perform better than the previous models because the eight experiments in the previous work included a lower number of tomograms (439) than the six experiments of the present analysis (599). Moreover, the previous analysis used a larger variety of rock types (Carrara marble, quartz monzonite, Westerly granite) than the current study (only Westerly granite). The different rock types produce different fracture distributions that may make predictions among all the rock types difficult. For example, the Carrara marble experiments produce a more uniform spatial distribution of fractures of more similar sizes immediately preceding failure than the Westerly granite or monzonite experiments (e.g., fig. 1 in McBeck et al., 2020). Indeed, models that predict the characteristics of fracture properties, such as the volume and aperture, using other characteristics in the marble experiments produce lower R^2 scores than models developed for the granite and monzonite rocks (McBeck et al., 2022a). Consistent with this idea, the characteristics identified as important to the model predictions, using the SHAP values, are similar among models developed for the different experiments analyzed in the current work (Table S3). For example, when s=1600 voxels, all the experiments except WG19 primarily rely on the Gini coefficient to predict the distance to failure. This consistency suggests that the varying pore fluid pressure, confining stress, and amount of preexisting damage does not change which characteristics are the most useful for predicting the distance to failure in these experiments. Other factors that we did not test in our experiments, such as the loading rate, may change these characteristics.

Another key difference between the present and previous analyses is the inclusion of more features in the present analysis, such as the Gini coefficient. The models in the present study developed using the first eigenvalue and Gini coefficient produce better predictions of the distance to failure than models developed with other subsets of features, such as the first eigenvalue and the orientation relative to the σ_1 direction, θ (Fig. 4a, c, e). This result suggests that the Gini coefficient provides useful information about the timing of macroscopic failure, and that adding this metric in the previous analysis may have improved the model performance.

When the models include data from all the experiments and only subsets of the fracture characteristics, the characteristics that produce the best performing models and thus contain the most useful information for predicting the timing of macroscopic failure, are the eigenvalues (proportional to the fracture length and aperture) and anisotropy (Fig. 4b, d, f). Models that include the volume of the fractures rank only

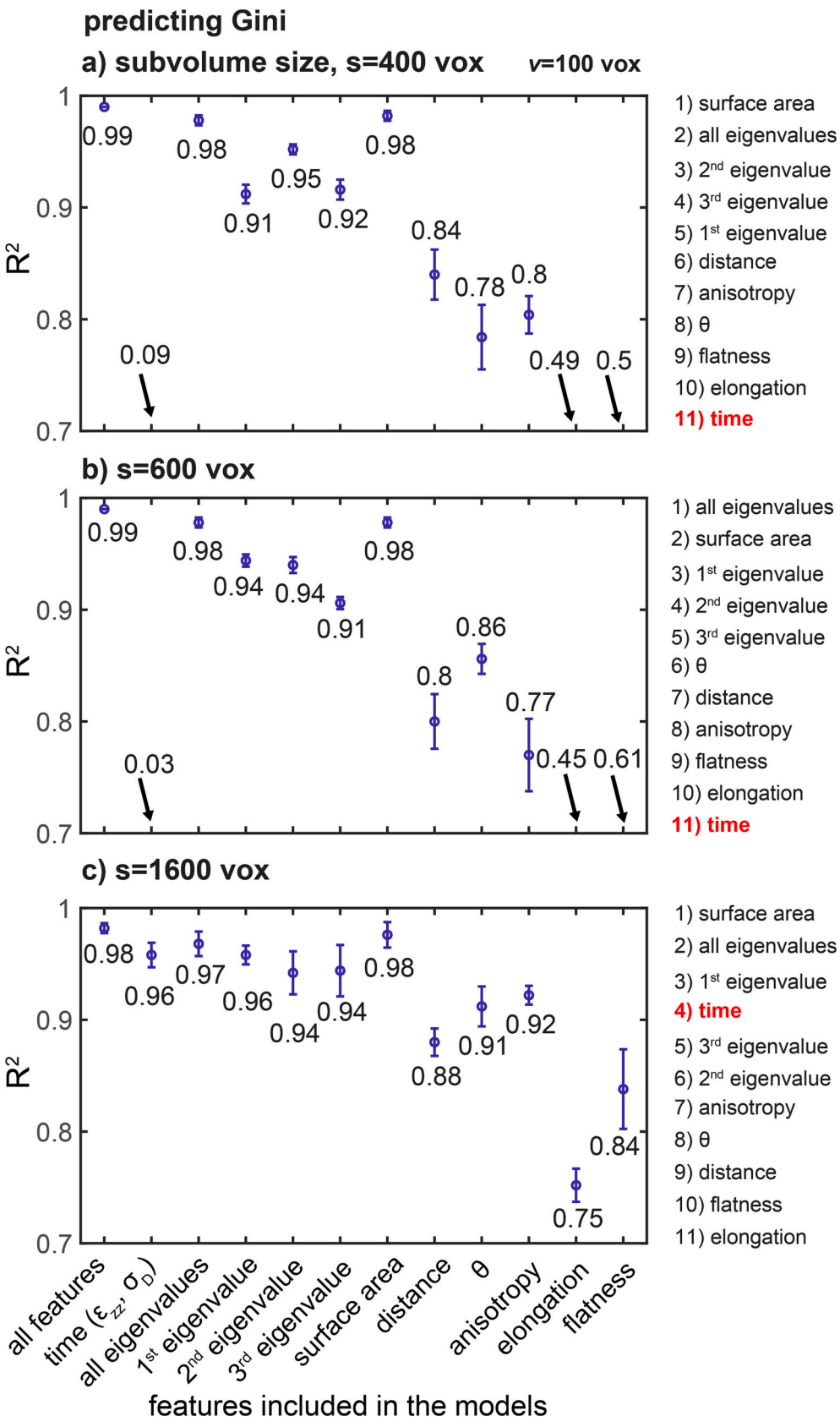

(caption on next page)

Fig. 7. Performance of models that predict the Gini coefficient using all the features, and only subsets of features with data from all the experiments for v=100 voxels and a) s=400 voxels, b) s=600 voxels, and c) s=1600 voxels. The model performance is reported as the mean ± one standard deviation of the R^2 values of models developed with different training and testing datasets. The text next to each data point is the mean R^2 value. The list to the right of each plot shows the ranking of the models, where one is the best-performing model. The models that use features that describe the time in the experiment (ε_{zz} and σ_D) are highlighted with red, bold font. When s=1600 voxels, the models that use the time-based features, ε_{zz} and σ_D, produce high R^2 values (c). For the smaller subvolumes, in contrast, these models perform poorly (a-b). (For interpretation of the references to colour in this figure legend, the reader is referred to the web version of this article.)

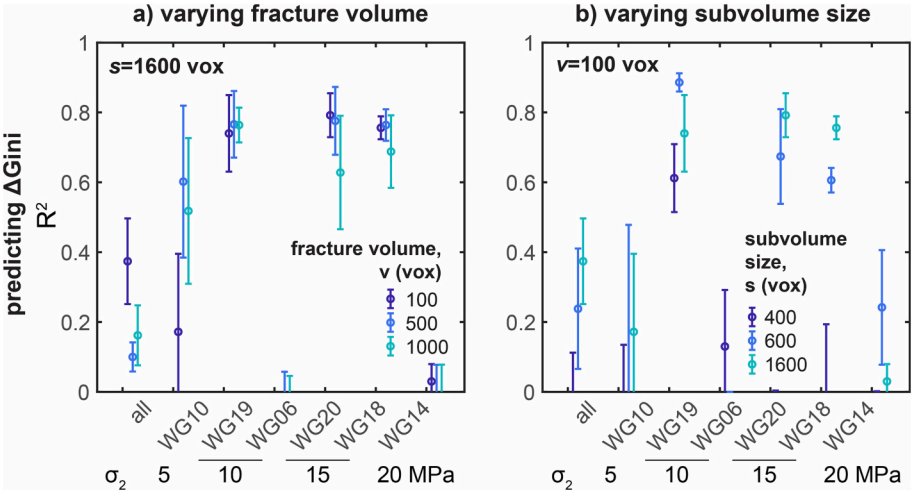

Fig. 8. Performance of models that predict the change in the Gini coefficient, ΔGini, from one differential stress step to the next using different combinations of the v (a), and s (b). Only three experiments produce reasonable model performances, with R^2 values >0.7: WG19, WG20, and WG18. These experiments do not include phases of delocalization.

fourth to sixth out of eleven, and models that include only the Gini coefficient or distance between the fractures rank only seventh to tenth out of eleven models. When the first eigenvalue is combined with other characteristics (Fig. 4 a, c, e), the top three or four characteristics that produce the best performing models are the volume, distance between fractures, anisotropy, and third eigenvalue (proportional to the aperture).

The characteristic that provides less useful information, particularly when it is combined with the fracture length, is the orientation of the fracture, θ. This result is surprising because the orientation is widely used in the Coulomb failure criterion, and calculations of the stress intensity factor (e.g., Jaeger and Cook, 1979; Paterson and Wong, 2005), and is often linked to the evolving micromechanisms of damage as rocks approach macroscopic failure (e.g., Tapponier and Brace, 1976). Consistent with the relative unimportance of θ identified here, a previous analysis that predicted fracture characteristics, such as θ, using other characteristics found that models that predict θ perform more poorly than models that predict the other characteristics (McBeck et al., 2022a). The apparent difficulty of predicting θ in this previous work, and the relative unimportance of θ when predicting the stress distance to failure in the current work, suggest that the relationship between θ and other characteristics, such as length, and the evolution of θ toward macroscopic failure is less systematic than other fracture characteristics.

The previous analysis that used fracture characteristics to predict the distance to failure found that the fracture volume is not useful for predictions, while the aperture, anisotropy, θ, and distance between fractures are useful for these predictions (McBeck et al., 2020). Both the previous and present analyses identified the aperture, anisotropy, and distance between fractures as important characteristics. The previous and present analyses differ in the relative importance of the fracture volume and θ. This difference may arise because of the inclusion of different rock types (monzonite and Carrara marble) in the previous work. The Carrara marble and Westerly granite produce fracture populations with different sizes and volumes for a given distance to failure that may cause the fracture volume to be a worse predictor of the distance to failure than the anisotropy, distance between fractures, or θ. In general, however, we consider the results of the present analysis to be more robust than the previous analysis because the present analysis produces higher R^2 scores. In both the present and previous work, one of the most important characteristics for the model predictions when combined with the other important characteristics is the distance between fractures. Consequently, the spatial distribution of the fractures is useful for predicting the timing of macroscopic failure in triaxial compression experiments on crystalline rocks at the stress and temperature conditions of the upper crust.

4.2. *Predictability of localization*

Previous analyses (e.g., Ben-Zion and Zaliapin, 2020, 2019) suggest that monitoring the spatial distribution of deformation, such as fractures or seismicity, may be useful for estimating the timing of catastrophic failure. To help such efforts, we developed machine learning models to predict the localization of the fracture networks. Previous studies have demonstrated that fracture networks, strain fields, acoustic emissions, and low magnitude seismicity can temporarily decrease in spatial localization as the system approaches catastrophic failure (Benson et al., 2007; McBeck et al., 2021a, 2022b; Ben-Zion and Zaliapin, 2020). Because the factors that control these phases of delocalization remain unclear, we developed models to predict the change in the localization from one stress step to the next.

The models that predict the Gini coefficient for individual experiments using the largest subvolume size primarily depend on features that describe the time in the experiment, including ε_{zz} and σ_D (Table S4). This consistency among the experiments suggests that the confining stress, fluid pressure, and amount of preexisting damage do not alter the usefulness of these features for predicting the localization of the fracture networks in these experiments. The models developed with all the experiments and the largest subvolume size primarily depend on the second eigenvalue, according to the SHAP values (Table S4). However, when these models only have access to subsets of features, they perform

with slightly higher R^2 values (0.96) when they only include the time-based features (ε_{zz} and σ_D) than when they only include the second eigenvalue (0.94) (Fig. 7c).

The performance of the models developed with different subsets of features is a more reliable measure of the relative usefulness of each characteristic to the predictions than the SHAP values. Consequently, for models developed with the largest subvolume size for all the experiments combined, and individual experiments, the time-based features produce some of the best predictions of the Gini coefficient. This result highlights the strong relationship between the localization of the fracture networks and the timing of macroscopic failure. This result is consistent with previous analyses that observed generally increasing localization preceding macroscopic failure in the fracture networks and strain fields of X-ray tomography triaxial compression experiments (McBeck et al., 2021a, 2022b), in low magnitude seismicity in southern and Baja California (Ben-Zion and Zaliapin, 2020), and in the spatial distribution of acoustic emissions in triaxial compression experiments (Lockner et al., 1991; Benson et al., 2007; Aben et al., 2019). The result is also consistent with theoretical results based on bifurcation theory (Rudnicki and Rice, 1975) and damage rheology models (Lyakhovsky et al., 2011) that describe macroscopic failure as a product of localization. In both bifurcation theory and damage rheology models, the deformation field separates into two solutions that represent the localized shear zone and surrounding material outside the shear zone during failure.

Two conceptual theories have been proposed to describe the evolution of deformation approaching system-size failure in rocks in the brittle regime. One theory suggests that brittle failure may be a critical phenomenon with power-law acceleration of damage before failure (e.g., Renard et al., 2018). Alternatively, bifurcation theory may determine the conditions at which deformation localizes and ultimately produces system-scale failure (e.g., Rudnicki and Rice, 1975). Recent work using two-dimensional cellular solids under compression indicates the compatibility of these two theories (Mayya et al., 2023). These experiments show that the approach to failure contains a phase of power-law acceleration of damage at some distance to failure, and then a bifurcation of the deformation field in the final stage of loading immediately preceding macroscopic failure, producing localization. If this approach applies to a wide range of brittle heterogeneous materials, such as rocks, then the final localization stage following the power-law acceleration of damage may be a deterministic precursor of system-size failure.

For the models that predict the change in localization, ΔGini, some models developed for individual experiments achieve moderate to strong correlations between the predicted and observed ΔGini (Fig. 8). However, these experiments host systematic increases in the Gini coefficient toward macroscopic failure, and no clear phases of delocalization (Fig. 5). The poor performance of models that predict ΔGini for experiments that include phases of delocalization illustrates the difficulty of predicting these temporary episodes. Moreover, the set of experiments that produce more poorly performing models do not differ in their initial conditions, such as confining stress, fluid pressure, or initial damage, from the experiments that produce better models. Consequently, future work is needed to identify the conditions that promote phases of delocalization.

The features that dominantly control the predicted ΔGini include ε_{zz} and σ_D for models using largest subvolume, and the flatness and eigenvalues of fractures for models using the smaller subvolumes (Table S5). The dependence of the models on the macroscopic time-based features is consistent with the observed acceleration of the Gini coefficient in these experiments (Fig. 5), which produce systematic increases in the ΔGini as a function of ε_{zz} and/or σ_D.

4.3. Implications for upscaling

A key question in this analysis is how to extend the results to larger length-scales, such as kilometer-scale crustal fault networks. To provide insights into upscaling, we varied the size of the system (i.e., subvolume size, s) used to calculate the fracture characteristics. In both the models that predict the distance to failure and the Gini coefficient for the individual experiments, varying s from the largest subvolume to one of the smaller subvolumes changes the features that most strongly control the model predictions identified with the SHAP values (Table S3, Table S4). However, comparing the performance of models that only include subsets of fracture characteristics reveals general similarities among the subvolume sizes for models developed with all the experiments (Fig. 4, Fig. 7).

For models that predict the distance to failure using all of the experiments, the fracture length (first eigenvalue) provides more useful information about the distance to failure, and thus produces better model performance, than the other tested characteristics, including the anisotropy, θ, Gini coefficient, and distance between the fractures, regardless of subvolume size (Fig. 4). When the fracture length is combined with the other fracture network properties to predict the distance to failure, the volume, anisotropy, and distance between fractures generally provide more useful information than the other tested characteristics for all the subvolume sizes.

One moderate difference between models that predict the stress distance to failure with different subvolume sizes is that the Gini coefficient produces better performing models at larger subvolume sizes compared to smaller subvolumes (Fig. 4). Similarly, for models that predict the stress distance to failure using the individual experiments, the Gini coefficient is one of the most important identified features for the larger subvolumes, but not the smaller subvolumes (Table S3). The relative unimportance of the Gini coefficient for the smaller subvolumes reflects the heterogeneity of the Gini coefficient calculated in the smaller subvolumes. In particular, the Gini coefficient in one subvolume can differ by a significant amount from the Gini coefficient in another subvolume at the same stress step (Fig. S3). In other words, the size of the representative elementary volume (e.g., Bachmat and Bear, 1987; Zhang et al., 2000; McBeck et al., 2023b) of the Gini coefficient is the size of the system or larger, rather than smaller than the system. This difference obscures the relationship between the Gini coefficient and the distance to failure, reducing the ability of the models to predict this relationship. This heterogeneity helps explain the better performance of models that predict the distance to failure using data from all the experiments developed with the first eigenvalue and Gini coefficient at larger subvolumes (Fig. 4e) compared to the performance of these models at smaller subvolumes (Fig. 4a, c).

Similar to models that predict the distance to failure, the models that predict the Gini coefficient primarily depend on the same subset of features at the varying subvolume sizes. In particular, the most important identified features include the eigenvalues, surface area, and distance between the fractures for all subvolume sizes (Fig. 7). For the largest subvolume size, the time-based features (ε_{zz} and σ_D) also produce some of the best-performing models. The difference in the importance of the time-based features with different subvolume sizes arises at least in part from the heterogeneity of the Gini coefficient described in the previous paragraph and in Fig. S3.

In summary, these results suggest that the fracture network characteristics that provide the most useful information about the distance to failure and the value of the Gini coefficient are generally independent of the system size. Consequently, we cautiously suggest that the results found at these smaller scales may apply to larger crustal systems. Although the length scale of these experiments is several orders of magnitude smaller than the length scales of crustal fault networks, the length distribution of fractures can be scale-invariant over several orders of magnitude (e.g., Bonnet et al., 2001). These scaling properties suggest that the fracture characteristics observed in the laboratory may be similar to characteristics observed in the crust. However, these scaling properties break down when the system includes a macroscopic, system-scale heterogeneity, such as a fault or mechanical contact between

lithographic units. Consequently, these results may be most applicable to volumes of crust without system-scale heterogeneities, such as the damage zone or host rock adjacent to a crustal fault.

For example, the fracture length and volume produce models that perform better than those developed from the fracture length and orientation (Fig. 4). Consequently, monitoring changes in the bulk fracture volume, such as with the seismic wave speeds (e.g., Chiarabba et al., 2020; Shreedharan et al., 2021a, 2021b) may be useful for forecasting the timing of large earthquakes, and identifying the preferred orientation of these fractures, through seismic anisotropy for example, may not significantly improve forecasting efforts.

5. Conclusions

The experimental results and machine learning models help improve our understanding of the evolving deformation leading to catastrophic failure. The models predict the distance to failure in terms of the differential stress, the localization of the fracture networks, and the change in localization using characteristics of the fracture networks observed in X-ray tomography triaxial compression experiments. The six experiments on Westerly granite include systematically varying confining stress, fluid pressure, and amounts of preexisting damage. The models produce better predictions of the stress distance to macroscopic failure than previous work (McBeck et al., 2020), with R^2 values of 0.8–0.95. This improvement in the model performance lends confidence to the idea that monitoring geophysical changes in the crust produced by the evolution of fracture network characteristics may assist earthquake early warning efforts. Examining the performance of models developed with subsets of characteristics helps identify features that may be the most useful to monitor in the crust.

The analysis indicates that the first eigenvalue of the fractures (proportional to the fracture length), fracture volume, distance between fractures, shape anisotropy (or thinness of the fractures), and third eigenvalue (proportional to the smallest aperture), provide the most useful information about the timing of macroscopic failure (Fig. 9a). The characteristic that provides less useful information, particularly when it is combined with the fracture length, is the fracture orientation relative to the σ_1 direction. These results are consistent for all the tested subvolume sizes, so we cautiously propose that monitoring changes in the bulk fracture volume, such as with the seismic wave speeds (e.g., Chiarabba et al., 2020) may be useful for forecasting the timing of large earthquakes, whereas identifying the preferred orientation of these fractures, through seismic anisotropy, may be less useful. The characteristics that are the most beneficial for the model predictions are generally consistent among models developed for the different experiments. This result suggests that the usefulness of these characteristics for predicting the timing of failure is independent of the confining stress, fluid pressure, and amounts of preexisting damage within the ranges of the parameters tested here.

Monitoring the spatial distribution of deformation, such as fractures or seismicity, may be useful for estimating the timing of catastrophic failure (e.g., McBeck et al., 2020; Kato and Ben-Zion, 2021). Although deformation generally localizes toward catastrophic failure, it occasionally decreases in localization (McBeck et al., 2021a, 2022b; Ben-Zion and Zaliapin, 2020) (e.g., Fig. 1), which complicates efforts to use localization to recognize the acceleration of the precursory stage leading to large earthquakes. To help such efforts, we developed machine learning models to predict the localization of the fracture networks as measured with the Gini coefficient of the fracture volume. The models can predict the Gini coefficient with R^2 values above 0.90, but predict changes in the Gini coefficient from one stress step to the next with R^2 values from below zero to 0.8 for individual experiments. The features that describe the macroscopic time in the experiment, ε_{zz} and σ_D, produce the best predictions of the Gini coefficient when models are developed using the complete scan at a given stress step, rather than

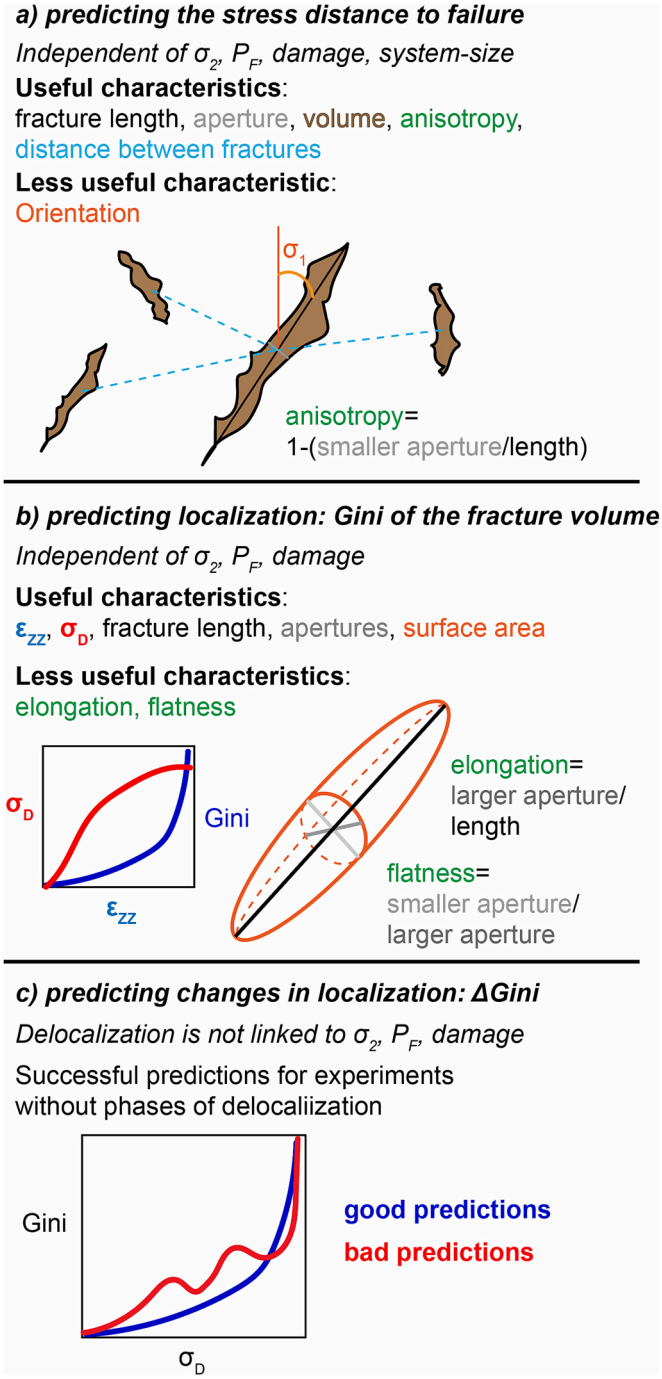

Fig. 9. Sketch of the key results of a) predicting the stress distance to failure, b) predicting the Gini coefficient, and c) predicting the change in the Gini coefficient. a) Independent of the stress and fluid conditions, amount of preexisting damage, and size of the system, the characteristics that are the most useful for predicting the distance to failure are the fracture length, aperture, volume, anisotropy, and distance between the fractures. In contrast, the orientation is less useful. b) Independent of the stress and fluid conditions, and amount of preexisting damage, but not of the system size, the characteristics that are the most useful for predicting the Gini coefficient are the macroscopic axial strain, differential stress, fracture length, apertures, and surface area. In contrast, the ratios between the apertures (elongation and flatness) are not as useful. c) Episodes of delocalization of the fracture networks are not linked to the confining stress, fluid pressure, and amount of damage. The models can predict the change in the Gini coefficient, and thus phases of localization and delocalization, for experiments that host fracture networks that systematically increase in localization, and do not host phases of delocalization.

subvolumes of the scan. This result applies for models developed using all the experiments and individual experiments (Fig. 9b). Consequently, these results highlight the clear relationship between deformation localization and the accumulated axial strain and/or differential stress in the experiment, and thus the proximity to macroscopic failure. The consistency of the importance of ε_{zz} and σ_D among the different experiments indicates that varying the stress and fluid conditions or preexisting damage does not perturb the relationship between localization and proximity to failure. This result is consistent with previous work that attributed macroscopic failure to the localization of deformation (e.g., Rudnicki and Rice, 1975; Lyakhovsky et al., 2011). The heterogeneity of the Gini coefficient, and thus the fracture networks (e.g., Fig. S3), explains the relative unimportance of the ε_{zz} and σ_D for predicting the Gini values at smaller subvolumes.

The models achieve moderate to strong correlations between the predicted and observed ΔGini for the experiments that do not include phases of delocalization, and weak to non-existent correlations for the experiments with phases of delocalization (Fig. 8, Fig. 5, Fig. 9c). These results highlight the difficulty of predicting these temporary episodes from the fracture network characteristics. The set of experiments that produce more poorly performing models do not differ in their initial conditions, such as confining stress, fluid pressure, or initial damage, from the experiments that produce better models. Consequently, additional analyses are required to constrain the conditions that promote phases of delocalization.

Credit Author statement.

JAM designed and performed research, contributed analytical tools, analyzed data and wrote the paper. YB-Z helped design research focus and write the paper. BC helped perform the experiments and write the paper. FR designed research, contributed analytical tools, helped perform the experiments, analyzed data and helped write the paper.

CRediT authorship contribution statement

Jessica McBeck: Writing – original draft, Visualization, Software, Project administration, Methodology, Funding acquisition, Conceptualization. **Benoît Cordonnier:** Writing – review & editing, Resources, Methodology. **Yehuda Ben-Zion:** Writing – review & editing, Investigation, Funding acquisition. **François Renard:** Writing – review & editing, Resources, Methodology, Funding acquisition.

Declaration of Competing Interest

The authors declare that they have no known competing financial interests or personal relationships that could have appeared to influence the work reported in this paper.

Data availability

The experimental data (time series of X-ray tomograms) are available on Norstore with DOI 10.11582/2023.00007

Acknowledgements

The Research Council of Norway (grant 300435 to JM), U.S. Department of Energy (grant DE-SC0016520 to YBZ), and the European Research Council under the European Union's Horizon 2020 research and innovation program (grant No. 101019628 BREAK to FR) funded this work. JM and FR acknowledge support from the project FricFrac funded by the Center for Advanced Study (CAS) at the Norwegian Academy of Science and Letters during academic year 2023-2024. Beamtime was allocated at the European Synchrotron Radiation Facility (Long Term Proposal ES-1190). The experimental data (time series of X-ray tomograms) are available on Norstore with DOI 10.11582/2023.00007 (https://archive.norstore.no/pages/public/datasetDetail.jsf?id=10.11582/2023.00007). The code used to build the machine learning models are available on Github (https://github.com/jmcbeck/Machine_Learning_Rock_Deformation).

Appendix A. Supplementary data

Supplementary data to this article can be found online at https://doi.org/10.1016/j.tecto.2023.230191.

References

Aben, F.M., Brantut, N., Mitchell, T.M., David, E.C., 2019. Rupture energetics in crustal rock from laboratory-scale seismic tomography. Geophys. Res. Lett. 46 (13), 7337–7344.
Ashby, M.F., Sammis, C.G., 1990. The damage mechanics of brittle solids in compression. Pure Appl. Geophys. 133, 489–521.
Atkinson, B.K., Meredith, P.G., 1987. Experimental fracture mechanics data for rocks and minerals. In: Fracture Mechanics of Rock, 477.
Bachmat, Y., Bear, J., 1987. On the concept and size of a representative elementary volume (REV). In: Advances in Transport Phenomena in Porous Media, pp. 3–20.
Bakun, W.H., Aagaard, B., Dost, B., Ellsworth, W.L., Hardebeck, J.L., Harris, R.A., Waldhauser, F., 2005. Implications for prediction and hazard assessment from the 2004 Parkfield earthquake. Nature 437 (7061), 969–974.
Benson, P.M., Thompson, B.D., Meredith, P.G., Vinciguerra, S., Young, R.P., 2007. Imaging slow failure in triaxially deformed Etna basalt using 3D acoustic-emission location and X-ray computed tomography. Geophys. Res. Lett. 34 (3), L03303.
Ben-Zion, Y., Zaliapin, I., 2019. Spatial variations of rock damage production by earthquakes in southern California. Earth Planet. Sci. Lett. 512, 184–193.
Ben-Zion, Y., Zaliapin, I., 2020. Localization and coalescence of seismicity before large earthquakes. Geophys. J. Int. 223 (1), 561–583.
Bieniawski, Z.T., 1968. Fracture dynamics of rock. Int. J. Fract. Mech. 4, 415–430.
Bolton, D.C., Marone, C., Saffer, D., Trugman, D.T., 2023. Foreshock properties illuminate nucleation processes of slow and fast laboratory earthquakes. Nat. Commun. 14 (1), 3859.
Bonnet, E., Bour, O., Odling, N.E., Davy, P., Main, I., Cowie, P., Berkowitz, B., 2001. Scaling of fracture systems in geological media. Rev. Geophys. 39 (3), 347–383.
Brace, W.F., 1964. Brittle fracture of rocks. In: State of Stress in the Earth's Crust, pp. 111–174.
Brace, W.F., Bombolakis, E.G., 1963. A note on brittle crack growth in compression. J. Geophys. Res. 68 (12), 3709–3713.
Brace, W.F., Paulding Jr., B.W., Scholz, C.H., 1966. Dilatancy in the fracture of crystalline rocks. J. Geophys. Res. 71 (16), 3939–3953.
Buades, A., Coll, B., Morel, J.M., 2005. A non-local algorithm for image denoising. In: 2005 IEEE Computer Society Conference on Computer Vision and Pattern Recognition (CVPR'05), 2, pp. 60–65.
Cartwright-Taylor, A., Main, I.G., Butler, I.B., Fusseis, F., Flynn, M., King, A., 2020. Catastrophic failure: how and when? Insights from 4-D in situ X-ray microtomography. J. Geophys. Res. Solid Earth 125 (8) e2020JB019642.
Chiarabba, C., De Gori, P., Segou, M., Cattaneo, M., 2020. Seismic velocity precursors to the 2016 Mw 6.5 Norcia (Italy) earthquake. Geology 48 (9), 924–928.
Dresen, G., Kwiatek, G., Goebel, T., Ben-Zion, Y., 2020. Seismic and aseismic preparatory processes before large stick–slip failure. Pure Appl. Geophys. 177, 5741–5760.
Fairhurst, C., Cook, N.G.W., 1966. The of maximum phenomenon of rock splitting parallel to the direction compression in the neighbourhood of a surface. In: 1st ISRM Congress, pp. 687–692.
Gini, C., 1921. Measurement of inequality of incomes. Econ. J. 31 (121), 124–125.
Horii, H., Nemat-Nasser, S., 1985. Compression-induced microcrack growth in brittle solids: axial splitting and shear failure. J. Geophys. Res. Solid Earth 90 (B4), 3105–3125.
Hulbert, C., Rouet-Leduc, B., Johnson, P.A., Ren, C.X., Rivière, J., Bolton, D.C., Marone, C., 2019. Similarity of fast and slow earthquakes illuminated by machine learning. Nat. Geosci. 12 (1), 69–74.
Jaeger, J.C., Cook, N.G.W., 1979. Fundamentals of Rock Mechanics, 3rd edn. Chapman & Hall, London.
Kandula, N., Cordonnier, B., Boller, E., Weiss, J., Dysthe, D.K., Renard, F., 2019. Dynamics of microscale precursors during brittle compressive failure in Carrara marble. J. Geophys. Res. Solid Earth 124 (6), 6121–6139.
Kato, A., Ben-Zion, Y., 2021. The generation of large earthquakes. Nat. Rev. Earth Environ. 2 (1), 26–39.
Lockner, D., Byerlee, J.D., Kuksenko, V., Ponomarev, A., Sidorin, A., 1991. Quasi-static fault growth and shear fracture energy in granite. Nature 350 (6313), 39–42.
Lundberg, S.M., Lee, S.I., 2017. A unified approach to interpreting model predictions. In: Advances in Neural Information Processing Systems, pp. 4765–4774.
Lyakhovsky, V., Hamiel, Y., Ben-Zion, Y., 2011. A non-local visco-elastic damage model and dynamic fracturing. J. Mech. Phys. Solids 59 (9), 1752–1776.
Marty, S., Schubnel, A., Bhat, H.S., Aubry, J., Fukuyama, E., Latour, S., Nielsen, S., Madariaga, R., 2023. Nucleation of laboratory earthquakes: quantitative analysis and scalings. J. Geophys. Res. Solid Earth 128 (3) e2022JB026294.
Mayya, A., Berthier, E., Ponson, L., 2023. How criticality meets bifurcation in compressive failure of disordered solids. Phys. Rev. X 13 (4), 041014.
McBeck, J.A., Aiken, J.M., Mathiesen, J., Ben-Zion, Y., Renard, F., 2020. Deformation precursors to catastrophic failure in rocks. Geophys. Res. Lett. 47 (24) e2020GL090255.

McBeck, J.A., Ben-Zion, Y., Renard, F., 2021a. Fracture network localization preceding catastrophic failure in triaxial compression experiments on rocks. Front. Earth Sci. 9, 778811.
McBeck, J., Ben-Zion, Y., Zhou, X., Renard, F., 2021b. The influence of preexisting host rock damage on fault network localization. J. Struct. Geol. 153, 104471.
McBeck, J.A., Cordonnier, B., Renard, F., 2021c. The influence of spatial resolution and noise on fracture network properties calculated from X-ray microtomography data. Int. J. Rock Mech. Min. Sci. 147, 104922.
McBeck, J., Aiken, J.M., Cordonnier, B., Ben-Zion, Y., Renard, F., 2022a. Predicting fracture network development in crystalline rocks. Pure Appl. Geophys. 179 (1), 275–299.
McBeck, J., Ben-Zion, Y., Renard, F., 2022b. Volumetric and shear strain localization throughout triaxial compression experiments on rocks. Tectonophysics 822, 229181.
McBeck, J., Cordonnier, B., Cooke, M., Fattaruso, L., Renard, F., 2023a. Deformation evolves from shear to extensile in rocks due to energy optimization. Commun. Earth Environ. 4 (1), 352.
McBeck, J.A., Cordonnier, B., Renard, F., 2023b. The evolving representative elementary volume size in crystalline and granular rocks under triaxial compression approaching macroscopic failure. Geophys. J. Int. 232 (3), 1898–1913.
Obreimoff, J.W., 1930. The splitting strength of mica. Proc. R. Soc. Lond. Ser. A Containing Papers of a Mathematical and Physical Character 127 (805), 290–297.
Paterson, M.S., 1958. Experimental deformation and faulting in Wombeyan marble. Geol. Soc. Am. Bull. 69 (4), 465–476.
Paterson, M.S., Wong, T.F., 2005. Experimental Rock Deformation: The Brittle Field, vol. 348. Springer, Berlin.
Pedregosa, F., Varoquaux, G., Gramfort, A., Michel, V., Thirion, B., Grisel, O., Blondel, M., Prettenhofer, P., Weiss, R., Dubourg, V., Vanderplas, J., Passos, A., Cournapeau, D., Brucher, M., Perrot, M., Vanderplas, J., 2011. Scikit-learn: machine learning in Python. J. Mach. Learn. Res. 12, 2825–2830.
Renard, F., Cordonnier, B., Dysthe, D.K., Boller, E., Tafforeau, P., Rack, A., 2016. A deformation rig for synchrotron microtomography studies of geomaterials under conditions down to 10 km depth in the Earth. J. Synchrotron Radiat. 23 (4), 1030–1034.
Renard, F., Weiss, J., Mathiesen, J., Ben-Zion, Y., Kandula, N., Cordonnier, B., 2018. Critical evolution of damage toward system-size failure in crystalline rock. J. Geophys. Res. Solid Earth 123 (2), 1969–1986.
Renard, F., McBeck, J., Cordonnier, B., Zheng, X., Kandula, N., Sanchez, J.R., Kobchenko, M., Noiriel, C., Zhu, W., Meakin, P., Fusseis, F., Dysthe, D.K., 2019a. Dynamic in situ three-dimensional imaging and digital volume correlation analysis to quantify strain localization and fracture coalescence in sandstone. Pure Appl. Geophys. 176 (3), 1083–1115.
Renard, F., McBeck, J., Kandula, N., Cordonnier, B., Meakin, P., Ben-Zion, Y., 2019b. Volumetric and shear processes in crystalline rock approaching faulting. Proc. Natl. Acad. Sci. 116 (33), 16234–16239.
Rizzo, R.E., Healy, D., Farrell, N.J., Heap, M.J., 2017. Riding the right wavelet: Quantifying scale transitions in fractured rocks. Geophys. Res. Lett. 44 (23), 11–808.
Rouet-Leduc, B., Hulbert, C., Lubbers, N., Barros, K., Humphreys, C.J., Johnson, P.A., 2017. Machine learning predicts laboratory earthquakes. Geophys. Res. Lett. 44 (18), 9276–9282.
Rudnicki, J.W., Rice, J.R., 1975. Conditions for the localization of deformation in pressure-sensitive dilatant materials. J. Mech. Phys. Solids 23 (6), 371–394.
Satoh, T., Shivakumar, K., Nishizawa, O., Kusunose, K., 1996. Precursory localization and development of microfractures along the ultimate fracture plane in amphibolite under triaxial creep. Geophys. Res. Lett. 23 (8), 865–868.
Shreedharan, S., Bolton, D.C., Rivière, J., Marone, C., 2021a. machine learning predicts the timing and shear stress evolution of lab earthquakes using active seismic monitoring of fault zone processes. J. Geophys. Res. Solid Earth 126 (7) e2020JB021588.
Shreedharan, S., Bolton, D.C., Rivière, J., Marone, C., 2021b. Competition between preslip and deviatoric stress modulates precursors for laboratory earthquakes. Earth Planet. Sci. Lett. 553, 116623.
Tang, C.A., Liu, H., Lee, P.K.K., Tsui, Y., Tham, L., 2000. Numerical studies of the influence of microstructure on rock failure in uniaxial compression—part I: effect of heterogeneity. Int. J. Rock Mech. Min. Sci. 37 (4), 555–569.
Tapponier, P., Brace, W.F., 1976. Development of stress induced micro-cracks in Westerly granite. Int. J. Rock Mech. Mining Sci. 13 (4), 103–112.
Vasseur, J., Wadsworth, F.B., Lavallée, Y., Bell, A.F., Main, I.G., Dingwell, D.B., 2015. Heterogeneity: the key to failure forecasting. Sci. Rep. 5 (1), 1–7.
Zhang, D., Zhang, R., Chen, S., Soll, W.E., 2000. Pore scale study of flow in porous media: scale dependency, REV, and statistical REV. Geophys. Res. Lett. 27 (8), 1195–1198.